Engineering Geology 289 (2021) 106186

Contents lists available at ScienceDirect

Engineering Geology

journal homepage: www.elsevier.com/locate/enggeo

Influence of the microstructure and roughness of weakness planes on the strength anisotropy of a foliated clay-rich fault gouge

J.M. Insua-Arévalo [a,*], M. Tsige [a], J.L. Sánchez-Roldán [a], E. Rodríguez-Escudero [a], J.J. Martínez-Díaz [a,b]

[a] Department of Geodynamics, Stratigraphy and Palaeontology, Complutense University of Madrid, Madrid, Spain
[b] IGEO: Geoscience Institute (UCM-CSIC), Madrid, Spain

ARTICLE INFO

Keywords:
Fault gouge
Triaxial tests
Anisotropy
Hoek&Brown strength criterion
Microstructure

ABSTRACT

Cataclastic rocks, as clay-rich fault gouges, are commonly present in brittle rock masses when fault zones appear during geological engineering projects. Highly deformed rocks that are of poor mechanical quality can lead to technical, safety, and economic problems in rock engineering. The aim of this study is to characterise the resistant behaviour of a highly deformed clay-rich gouge >40 m wide with a marked tectonic fabric that indicates strength anisotropy. We present the results of consolidated-undrained (CU) triaxial tests that were performed at low confining pressures (50, 150, and 300 kPa) on several sets of foliated gouge specimens with four different orientations in the tectonic fabric. Specimens were collected from the encapsulated rock cores of two research boreholes drilled through the Alhama de Murcia Fault (AMF), a main regional fault located in SE Spain. The strain–stress relationships and failure modes were established, indicating that the gouge behaves as hard soil or very soft rock. The test results were adjusted at each orientation using the non-linear Hoek and Brown criteria by considering the fault gouge as an *intact material* or as a *tectonised rockmass*. Here, we use the Geological Strength Index (GSI) as an indicator of the rockmass strength that depends on the direction of the tectonic fabric. However, the results from specimens with tectonic fabric that is oriented most favourably for failure were not the weakest in terms of rock strength. Such an anomalous result could be the result of asymmetry in the roughness of the weakness planes that is related to the original gouge microstructure characterised by the strong reorientation of clays in an S-C′ like tectonic fabric.

Our results will be useful for practical applications that are related to the stability of slopes and/or shallow underground excavations in brittle fault zones, and provide an inexpensive and easy way to preliminarily evaluate the anisotropic behaviour of this type of brittle fault zones for future engineering projects.

1. Introduction

The presence of fault zones in brittle rocks targeted by engineering geology or mining projects can be decisive when considering technical and economic feasibility (e.g. Brenner Base Tunnel, Alps, Austria, Sausgruber and Brandner, 2003; Guadarrama Base Tunnel, Central System, Spain, López Sopeña, 2005; Schubert et al., 2006; Coal mining support, Huainan, China, Kang et al., 2018). Cataclastic rocks as fault gouges are commonly present in fault zones affecting brittle rocks and always have very poor mechanical quality, leading to problems in rock engineering. Although gouges could be considered stiff soils, fault gouges usually comprise tectonically induced fabrics, implying anisotropic mechanical behaviour within bands reaching a width of up to 500 m (Julià and Santanach, 1998). Hence, the accurate determination of the anisotropic properties of gouges is critical when a reliable estimation of strength is required for defining proper constitutive equations for underground excavation, rock slope stability, or the bearing capacity at the foundations of rock masses.

The anisotropy of different intact rock and/or rock masses has been widely addressed (for example, Attewell and Sandford, 1974; Hoek and Brown, 1980; Ramamurthy et al., 1993; Saroglou and Tsiambaos, 2008; Ismael and Konietzky, 2019). However, the anisotropy in the mechanical behaviour of cataclastic rocks, such as fault gouges, has not yet been studied in depth. One of the main reasons for this is that it is difficult to characterise such rocks because of the difficulties that arise in: i) obtaining undisturbed samples during field investigations, ii) specimen

* Corresponding author at: C/José Antonio Nováis, 12, 28040 Madrid, Spain.
E-mail address: insuarev@ucm.es (J.M. Insua-Arévalo).

https://doi.org/10.1016/j.enggeo.2021.106186
Received 28 August 2020; Received in revised form 3 May 2021; Accepted 6 May 2021
Available online 11 May 2021

preparation, and iii) performing appropriate tests in the laboratory (Habimana et al., 2002), especially when specimens with different orientations are required. For this reason, much of the research investigating the mechanical behaviour of fault gouges has been based on remoulded samples (e.g. Morrow et al., 1982; Bao et al., 2020) or indirect probabilistic prediction models (Liu et al., 2007), and only a few studies in the literature have been based on undisturbed gouge samples (e.g. Scott et al., 1994). The frictional properties of fault gouges have been widely studied because of their relationship with the seismogenic behaviour of active faults. Frictional experiments examining the fault gouges in the Alhama de Murcia Fault (AMF) in SE Spain, which were investigated in this study, have previously been performed by Niemeijer and Vissers (2014) and Rodríguez-Escudero (2017). However, neither of these studies specifically investigated the anisotropic properties of the gouge.

Soft rocks have a mechanical behaviour that is similar to that of overconsolidated soil, and linear failure criterion (Mohr–Coulomb) can properly define the strength of a gouge. However, a geomechanical characterisation of cataclastic rocks carried out by Habimana et al. (2002), quantified the intensity of the tectonic degradation process using the Geological Strength Index (GSI) to suggest an extended nonlinear Hoek and Brown failure criterion. The general Hoek and Brown (H&B) criterion for rock masses is widely accepted and has been applied in many projects around the world involving underground excavation, engineering slope stability, mining, and major foundation engineering (i.e. dams). The H&B criterion was introduced in 1980 for the design of underground rock excavations. The criterion now incorporates both intact rock and discontinuities, which are characterised by the GSI into a system designed to estimate the mechanical behaviour of the typical rock masses encountered in tunnels, slopes, and foundations. The strength and deformation properties of intact rock, which have previously been derived using laboratory tests, are reduced based on the properties of discontinuities in a rock mass. The use of the H&B strength criterion implies the use of the GSI, which is a quick and simple index to obtain compared with expensive and tedious laboratory tests, especially for anisotropic rocks. Another advantage of using the H&B criterion is that it can also be applied to evaluate the failure of brittle materials such as rock matrix. In this case, the criterion considers micro-cracks or flaws in the intact material as grain boundaries or intergranular tensile cracks that propagate from their tips when frictional sliding occurs along the flaw (c.f. Hoek and Brown, 2019). Although H&B is primarily intended for use in isotropic rocks, anisotropic rocks have been evaluated by considering the variation of the H&B parameters depending on the strength anisotropy of the intact rock (e.g. Colak and Unlu, 2004; Saroglou and Tsiambaos, 2008).

This paper presents the results of triaxial tests that were performed on undisturbed core samples from a fault gouge in the AMF, for which specimens were prepared at four different orientations of the tectonic fabric to characterise the strength anisotropy. A detailed mineralogical and microfabric study was conducted, in addition to core scanning and image processing, to evaluate the influence of the roughness geometry on the weakness planes. Our results reveal that in addition to the angle of orientation between the main stress and the weak planes, the strength anisotropy of the foliated fault gouges can also be controlled by the roughness geometry of the weak planes along the direction of the displacement that was induced during the triaxial tests. The results have also been assessed using the non linear Hoek Brown failure criterion, including sensitivity to the Geological Strength Index (GSI). The results achieved in this study enhance the understanding of the mechanical behaviour of fault gouges, which will provide more accurate parameters for projects in which large infrastructure is designed.

2. Geological frame

The Alhama de Murcia Fault (AMF) is an active fault located in SE Spain (Fig. 1).

The AMF is an 87 km long, N040E–N065E, left-lateral strike-slip fault with a reverse component that dips 60–70° towards the NW. The damaging Lorca Mw 5.2 earthquake that occurred on 11 May 2011 was generated by the reactivation of a fault in a small section of the AMF (Martínez-Díaz et al., 2012). This fault developed as an approximately 20–30 m thick highly deformed clay-rich gouge with a strongly marked tectonic fabric (foliated gouge), denoting notable anisotropy. The fault gouge is formed mainly of quartz and muscovite/illite with minor

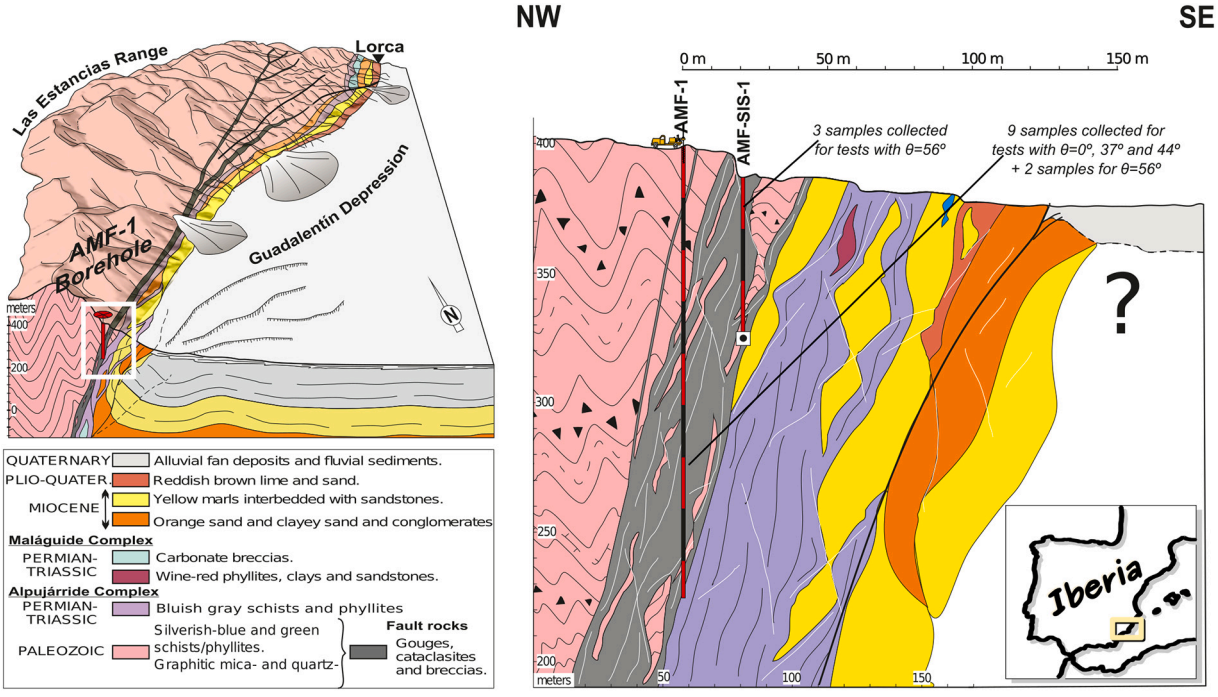

Fig. 1. Block diagram showing the local geology of the Alhama de Murcia Fault (AMF) and the situation of the boreholes AMF-1 and AMFSIS-1. The tested specimens were taken and prepared from undisturbed samples within the borehole cores.

proportions of kaolinite, carbonates, paragonite, and feldspar proportions (Tsige et al., 2017; Rodríguez-Escudero, 2017). The presence of graphite is notable because it influences the frictional properties (Rodríguez-Escudero et al., 2018). In addition to this macroscale fabric, the fault gouge presents a microscale structure that is characterised by the strong reorientation of the clay, which can play an important role in its elastic properties and strength. The tectonic fabric of the fault gouge is defined by C-C′-S planes that indicate a ductile style of deformation (Rutter et al., 1986; Rodríguez-Escudero et al., 2020) (Fig. 2A). The C′ planes are the most penetrative having the greatest control on weakness planes. All the minerals present within the gouge come from the schists and phyllites from the metamorphic basement of the upthrown block which constitute the protolith. This protolith, which is much more resistant, has a net contact with the fault gouge, marked by a clear mechanical contrast.

3. Experimental work

3.1. Sampling

The tested samples were collected from the cores of the research boreholes AMF-1 and AMF-SIS-1. The scientific AMF-1 borehole, collared on the up-thrown block of the fault, reaches a depth of 174 m (Fig. 1) (Martínez-Díaz et al., 2016). Wireline vertical drilling and coring were chosen to favour the recovery of high-quality fresh rock core. The fault gouge was encountered at a depth of 64 m and more than 100 m of high-quality fault rock core samples with diameters of 83 mm (PQ-3 size) were obtained. Eleven specimens were collected for testing from encapsulated rock cores at depths of 152–158 m (Table 1) to guarantee undisturbed and unweathered samples. However, the samples may have been altered to some extent as stress release and other disturbances are likely to occur during core drilling and exhumation (Rodríguez-Escudero et al., 2020).

The borehole AMF-SIS-1 is located several tens of meters east of AMF-1 and was drilled for seismic monitoring purposes. AMF-SIS-1 is 40 m in depth and was drilled vertically through the fault gouge (Fig. 1). Encapsulated rock core samples measuring 83 mm in diameter (PQ-3 size) were obtained. Three samples were selected from between 12 and 13 m deep (Table 1).

At the sites where the boreholes were drilled, the deformation in the fault is concentrated in a unique branch of the AMF where a constant orientation of N045E dips at 70° NW (Fig. 1). The main planes that occur in the specimens from this region are C′ planes, which are parallel planes with the greatest persistence (several centimetres to decimetres) within the tectonic fabric (Fig. 2). S planes link the C′ planes with a sigmoidal shape. The C planes are parallel to the limits of the entire fault shear zone and are not present at the size of the tested samples. Note that the dip of the C′ planes (56°) is different from that of the C planes (70°).

3.2. Specimen preparation

A total of 14 specimens were prepared for testing, which were grouped into four sets with different C′ plane orientations (Table 1): $\theta = 0°$ (three specimens), 37° (three specimens), 44° (three specimens), and 56° (five specimens), where θ is the angle between the direction perpendicular to the C′ plane and the orientation of the axial load (Fig. 2B).

Specimens were carefully hand-carved to form cylinders (Fig. 3) that were 74 ± 2 mm in height and 37 ± 1 mm in diameter (ASTM D 4767-95, 1995) . The axes of the $\theta = 56°$ specimens coincide with the vertical axis. Five specimens were tested with this orientation, three of which were collected from AFM-SIS-1 and two from the AFM-1 boreholes to avoid potentially biased results due to gouge heterogeneity. The axes of the specimens at $\theta = 37°$ and 44° are horizontal, with an angle of 15° between the trends of their long axes. The specimens with $\theta = 0°$ were prepared with the axis orientation perpendicular to the C′ planes (Table 1). Some of the tests were performed after re-saturation following notable drying out (i.e. samples with bulk degree of saturation < 30%) which may have influenced the strength properties of the samples, as the materials contain clays. This fact was considered when analysing the results.

3.3. Testing procedure

To characterise the failure criterion and stress–strain relationship, consolidated undrained (CU) triaxial tests were carried out on each of the four sets of specimens, each with a specific fabric orientation (Table 1). Tests were performed at two laboratories: 1) The Engineering Geology Lab at the Complutense University of Madrid (UCM) and 2) Geotecnia 2000. All the tests were conducted with a back pressure of 600 kPa, and saturation was achieved during consolidation (Skempton's B parameter = 1). The specimens were tested under different confining pressures: $\sigma_3 = 50$, 150, and 300 kPa using an axial strain rate of either 0.04 or 0.2 mm/min to favour the pore pressure balance. Additional tests at $\sigma_3 = 50$ and 300 kPa were performed on two extra specimens with $\theta = 56°$ to avoid possible biases associated with site or depth. CU triaxial tests allow the variation in the pore water pressure to be measured and registered during testing, meaning that the results can be considered in terms of effective stress (σ'_1 and σ'_3). In addition, the variation in the pore water pressure shows volume changes during testing, which was analysed using Skempton's A parameter. Such a low confining pressure is preferred as the anisotropy decreases as the confining pressure increases (e.g. Ramamurthy et al., 1993; Habimana et al., 2002). Using a low confining pressure also allows the nonlinear strength criterion of H&B to be utilized, which is applicable if the brittle–ductile limit is not exceeded (Hoek and Brown, 2019).

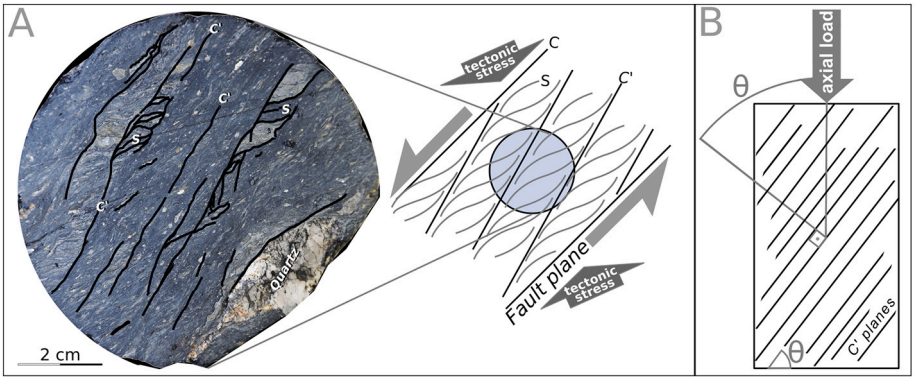

Fig. 2. A) Tectonic fabric of the fault gouge with C-C′-S planes in an 83 mm core section (PQ-3 size) viewed from the top. B) The angle θ defines the orientation of the axial load in relation to the direction perpendicular to the weakness planes (C′ planes) within the tested specimens.

Table 1
Sample data. θ is the angle between axial stress (σ_1) and the perpendicular direction to the weakness planes. UCM: University Complutense of Madrid. See Fig. 1 for location, Fig. 2B for spatial orientation of the weakness planes for the triaxial tests, Fig. 4 for failure angle (α), and Fig. 14 for the geometric relationships, in which the roughness of the C′ planes is also considered. Photos of the specimens after completion of the testing, except for TO-38-2, TT-1 and TT-2, are shown in Appendix A: Supplementary Data. Also note that failure angle α is absent where photographs are missing.

Specimen Lab ID	Location		Sample properties						Triaxial test						Geometric relationships			
			Unit weight (kN/m^3)			Moisture content (%)		Saturation (%)		Test conditions					Specimen axis orientation		Difference between the line of maximum dip and the profile of roughness	
	Borehole	Depth (m)	Dry	Bulk	Sat.	Bulk	Sat.	Bulk	Testing Lab.	Axial loading rate (mm/min)	Back pressure (kPa)	Confining pressure, σ3 (kPa)	Angle θ	Failure angle, α	Trend	Plunge	with the minimum roughness	with the maximum roughness
TO-P-1	AMF-1	158.04	21.04	21.20	23.13	0.7	9.9	7.3	UCM	0.04	600	50	0°	59°	135°	34°	–	–
TO-P-2	AMF-1	158.11	21.27	21.36	23.27	0.5	9.4	4.8	UCM	0.04	600	150	0°	58°	135°	34°	–	–
TO-P-3	AMF-1	158.18	21.64	22.18	23.51	2.5	8.6	28.8	UCM	0.04	600	300	0°	62°	135°	34°	–	–
TO-38-1	AMF-1	152.20	20.66	22.66	22.89	9.7	10.8	90.0	Geotecnia-2000	0.20	600	50	37°	61°	150°	00°	56°	34°
TO-38-2	AMF-1	152.50	20.73	22.77	22.93	9.9	10.6	92.9	Geotecnia-2000	0.20	600	150	37°		150°	00°	56°	34°
TO-38-3	AMF-1	152.80	20.85	22.83	23.01	9.5	10.3	92.1	Geotecnia-2000	0.20	600	300	37°	59°	150°	00°	56°	34°
TO-15-1	AMF-1	157.83	21.69	21.94	23.54	1.2	8.5	13.8	UCM	0.04	600	50	44°	58°	165°	00°	36°	54°
TO-15-2	AMF-1	157.94	20.97	21.13	23.08	0.8	10.1	7.6	UCM	0.04	600	150	44°	61°	165°	00°	36°	54°
TO-15-3	AMF-1	157.99	21.80	21.85	23.61	0.2	8.3	2.9	UCM	0.04	600	300	44°	58°	165°	00°	36°	54°
TT-1	AMFSIS-1	12.95	20.73	22.75	22.93	9.8	10.6	92.1	Geotecnia-2000	0.20	600	50	56°		000°	90°	81°	9°
TT-2	AMFSIS-1	13.05	21.01	23.09	23.10	9.9	10.0	99.5	Geotecnia-2000	0.20	600	150	56°		000°	90°	81°	9°
TT-3	AMFSIS-1	13.15	20.42	22.38	22.73	9.6	11.3	84.8	Geotecnia-2000	0.20	600	300	56°	56°	000°	90°	81°	9°
TT-1-bis	AMF-1	158,28	20.89	21.11	23.03	1.07	10.3	10.4	Geotecnia-2000	0.20	600	50	56°	59°	000°	90°	81°	9°
TT-3-bis	AMF-1	158,38	21.28	21.50	23.28	1.03	9.4	11.0	Geotecnia-2000	0.20	600	300	56°	56°	000°	90°	81°	9°

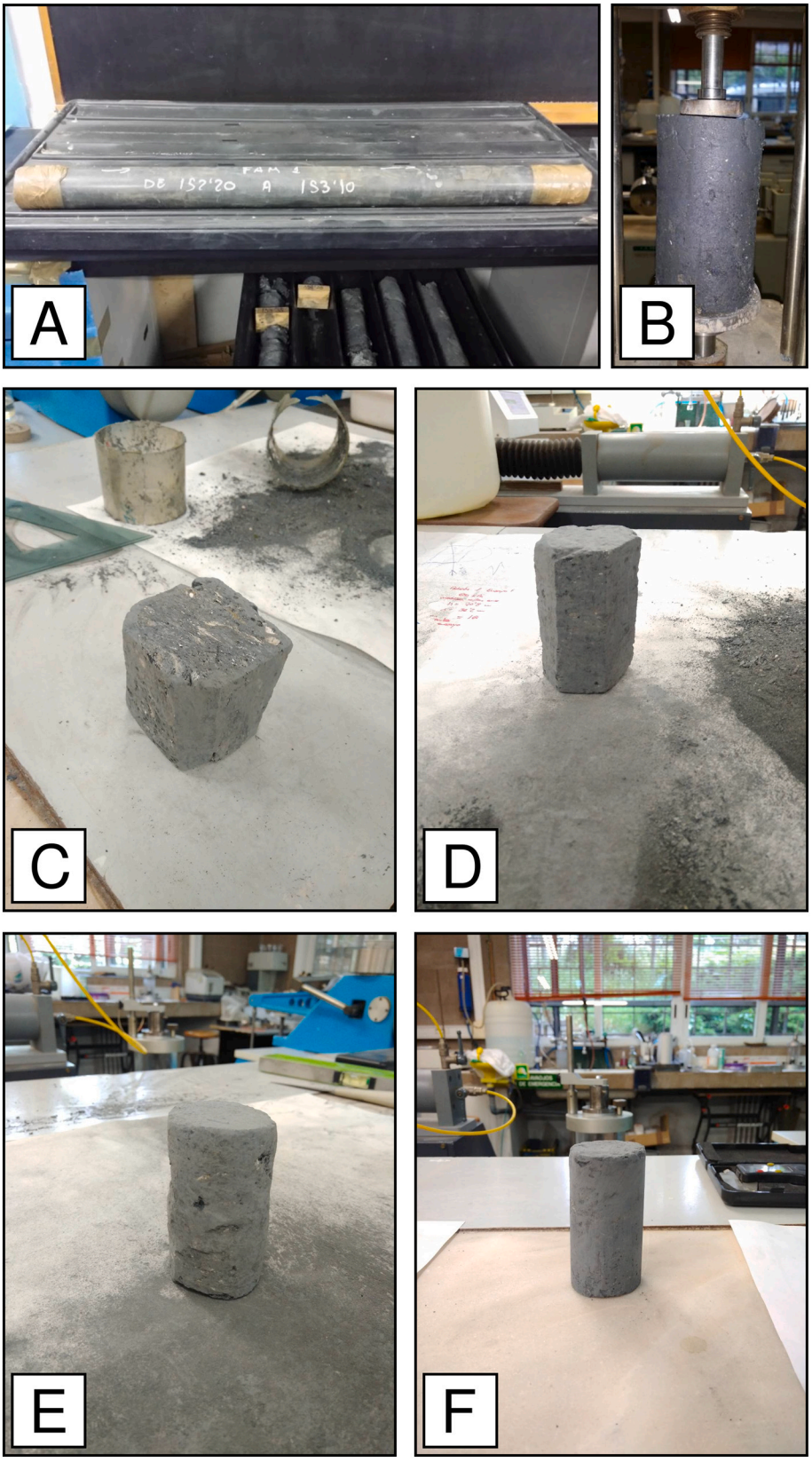

Fig. 3. Process of hand carving the tested specimens. First, (A) a depth interval from the encapsulated rock core samples was selected and (B) a sample of the required size was extracted. (C and D) The sample was then hand carved to reduce the excess volume and (E) a pseudo-cylindrical volume was obtained. (F) The final shape of the specimen was achieved after fine-tuning with sandpaper and files.

3.4. Mineralogical and microstructural analysis

To evaluate the influence that the intrinsic compositional and structural properties of the studied specimens have on the strength, the mineralogical and microstructural features of the fault gouge were studied. For the mineralogical study, samples of the bulk rock from both protoliths (Palaeozoic schists–phyllites from the Alpujárride Complex) and the fault gouge were prepared as powders of the bulk rock and the oriented aggregate of clay with a size fraction of <2 μm was separated by sedimentation following Stokes' Law to enhance the intensities of the peaks and aid in the identification of the clay mineral phases (Moore and Reynolds, 1997). The identification of each phase was performed by combining the X-ray diffraction patterns of three states: air dried, glycolated, and heated at 550 °C for 2 h. The relative abundances of the clay minerals were calculated using the method by Biscaye (1965).

The microstructure was analysed using a scanning electron microscope (SEM, JSM 6335F SEM CamScan Optics) at 10–20 kV, which was equipped with an energy dispersive X-ray analyser (EDAX) to determine the chemical composition. The samples were prepared to be perpendicular and parallel to mesoscopic foliation (to the main C′ planes). Owing to the brittle nature of the fault gouge, the thin sections and small irregular shape block samples were indurated by epoxy in a vacuum chamber before observation, following the method described by Rodríguez-Escudero (2017).

4. Experimental results

4.1. Failure modes

We observed three types of failure modes in the specimens, which depended on the orientation of the tectonic fabric: (i) failure through intact rock, (ii) failure along the foliation, and (iii) a mixed mode (Fig. 4 and photos in Appendix A: Supplementary Data). Specimens with $\theta = 0^\circ$ demonstrate a net fracture with a narrow band of deformation running throughout the intact rock. The angle of the fracture plane has an inclination of approximately 62°. Specimens with $\theta = 56^\circ$ also have a net fracture (with a narrower band of deformation); and the failure occurs along the weakness planes. The other two specimens with $\theta = 37^\circ$ and 44° present several planes of fractures within a wider band of deformation, with an angle of inclination of 58–59°. In this case, some of the fracture planes cut the C′ planes obliquely, while others run along the planes (mixed failure mode). It is also noticeable that these specimens present a final barrel shape (Fig. A2), indicating more ductile-like behaviour than that shown at the other orientations (0^0 and 56^0) with more brittle-like behaviour.

4.2. Strain–stress relationships

The results from the four sets of triaxial tests are presented in Fig. 5. The axial total stress (σ_1) increased with confining pressure in all tests except where $\theta = 44^\circ/\sigma_3 = 300$ (TO-38-3) (Fig. 5A). Variations in the axial load that result from deformation produces a pseudo-hyperbolic shape without a clear maximum value, as the axial load continues to increase in association with the deformation. This pattern implies a general ductile response in the heavily tectonised rock mass (Habimana et al., 2002), and could also imply strain hardening behaviour of the samples (Morrow et al., 1982). The pore water pressure (u) also increases with the confining total pressure, showing a similar pattern in all tests, which increases rapidly until the maximum values of approximately 1–3% deformation are reached, after which it decreases to reach negative values beyond >5% deformation.

In order to assess the deformational behaviour in more detail, we plotted the effective stress relationship (σ'_1/σ'_3) and Skempton's A parameter (Skempton, 1954) with the axial deformation (Fig. 5B). Both the σ'_1/σ'_3 ratio and the variation in the ratio were found to be inversely proportional to the confining pressure. Three specimens $\theta = 0^\circ/\sigma_3 = 150$ (TO-P-2), $\theta = 44^\circ/\sigma_3 = 150$ (TO-38-2), and $\theta = 56^\circ/\sigma_3 = 50$ duplicated (TT-1-bis) did not fit this pattern, probably because of the heterogeneity

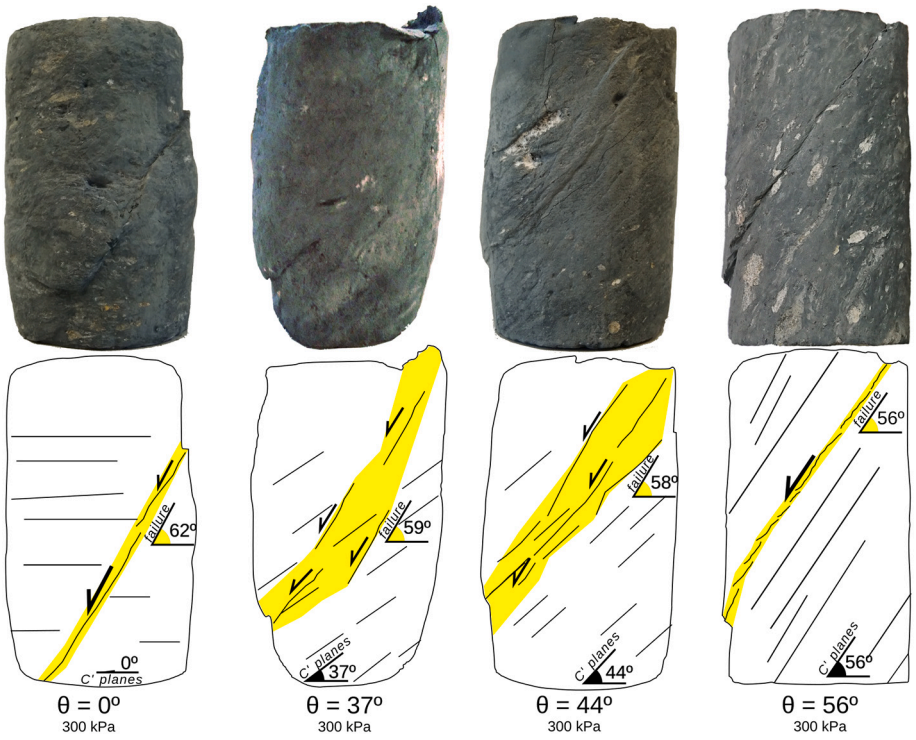

Fig. 4. Specimens tested using the CU triaxial test after failure. Four different C′ plane orientations were considered: $\theta = 0^\circ$, 37°, 44°, and 56°. The angle of the failure planes (α) within the failure band are marked in yellow (For scale: samples 74 ± 2 mm high). (For interpretation of the references to colour in this figure legend, the reader is referred to the web version of this article.)

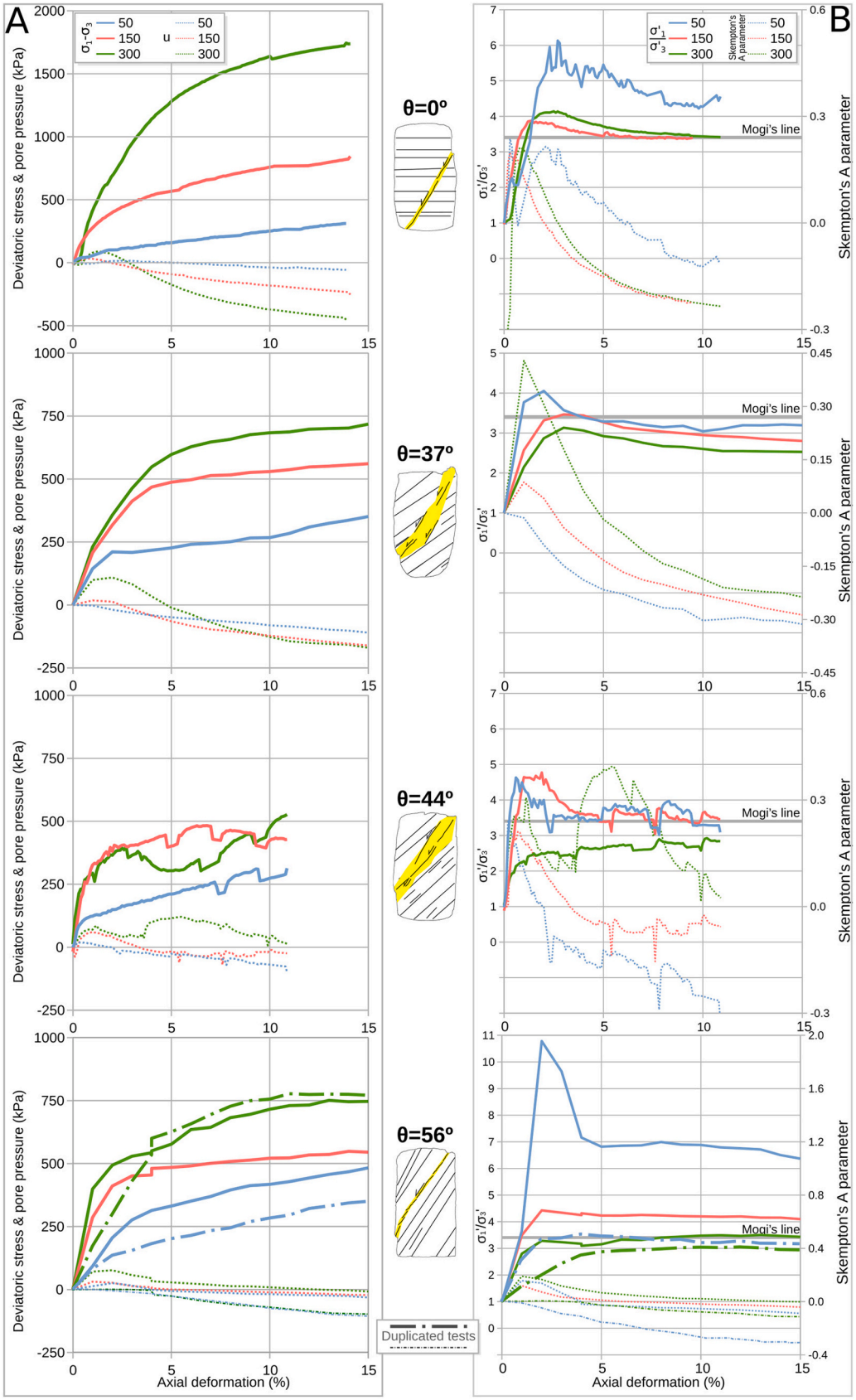

Fig. 5. Results from the triaxial tests at each orientation ($\theta = 0°$, 37°, 44°, and 56°). A: Variation in the deviatoric stress (σ_1-σ_3) and pore water pressure (u) with axial deformation (%) for each confining pressure (σ_3 = 50, 150, and 300 kPa). B: Variation in the effective stress relationships (σ'_1/σ'_3) and the Skempton's A parameter with deformation for each confining pressure.

in the mineralogy and the microstructure of the fault gouge (see Section 6). The results from these three specimens were therefore discarded for the subsequent strength analysis. On the other hand, all specimens show a general variation in mechanical behaviour from brittle to ductile as the confining pressure increases (Mogi's line in Fig. 5B), although samples with $\theta = 0^\circ$ show a σ'_1/σ'_3 ratio that always lies above Mogi's line. This reflects the failure modes considered in Section 4.1. and illustrated in Appendix A.

The maximum values of σ'_1/σ'_3 in all the tests (Fig. 5A) were reached at the yield point, that is, at the elastic to plastic behaviour transition, following the maximum pore water pressure (Bieniawski, 1967). Such an effect is also shown by Skempton's A parameter, which was experimentally determined from the relationship between the variation in the pore pressure (u) and the variation in the deviatoric stress (σ_1-σ_3), following the equation:

$$Skempton'sAparameter = \frac{\Delta u}{\Delta(\sigma_1 - \sigma_3)}$$

This parameter has positive values when contraction occurs and negative values when dilation occurs. In our tests, the Skempton's A parameter shows the maximum positive values early in the deformation. These peaks mark the onset of a stage in which the crack growth is stable, generating a relative dilation (Zhao and Cai, 2010). Once the yield point is reached, the A parameter presents values that are close to zero or even negative, denoting a stage of absolute dilation that is related to unstable crack growth (Bieniawski, 1967; Zhao and Cai, 2010).

5. Strength criteria

5.1. Failure occurrence

The failure occurrence must be determined to define the strength criteria for a studied fault gouge. As described above, the variation in the axial load that occurs with deformation shows a general pseudo-hyperbolic shape in which the axial load continuously increases with the deformation in most of the tests, not showing a clear peak (Fig. 5A). We consider that failure occurs at the maximum value of the σ'_1/σ'_3 relationship (yield point) because this is the point at which unstable fractures start to propagate (Bieniawski, 1967; Zhao and Cai, 2010), which is independent of the subsequent deformational behaviour. The effective principal stresses used to estimate the failure criteria are shown in Table 2. The maximum σ'_1/σ'_3 values were achieved at a range of deformation between 1% and 3%.

Nonetheless, in order to assess the uncertainty in taking the maximum σ'_1/σ'_3 values as a failure point, three other options were considered: (i) analysis of the σ'_1 vs σ'_3 paths, (ii) the stress values at maximum deformation (12.5%), and (iii) the stress values at several intermediate arbitrary deformation values (5%, 7.5%, and 10%). A simple linear adjustment was considered for the failure criterion in all options.

Several possible linear adjustments are observed in the σ'_1 vs σ'_3 paths (i) (Fig. 6) once the anomalous specimens described above ($\theta = 0^\circ/\sigma_3 = 150$, $\theta = 44^\circ/\sigma_3 = 150$, and $\theta = 56^\circ/\sigma_3 = 50$ duplicated) are discarded.

Reliable adjustments consider the maximum (tangent) or minimum (partially secant) envelopes for every set of tests. The envelopes are compared in Fig. 7A. The envelopes that consider (ii) stress values at maximum deformation (12.5%), and (iii) stress values at several intermediate arbitrary deformations (5%, 7.5%, and 10%), are displayed in Fig. 7B, together with the linear envelope associated with the maximum σ'_1/σ'_3 values (yield points). In relative terms, all envelopes have a similar pattern regardless of the option considered justifying the selection of the maximum σ_1/σ_3 ratio as the failure point.

The drying out and re-saturation of the samples with $\theta = 0^\circ$ and $\theta = 44^\circ$ (see Table 1) do not seem to have a significant influence on their strength properties, as both maximum and minimum values of resistance are achieved for these specimens, respectively.

Regarding the linear failure envelopes obtained from any of the options considered (Fig. 7), the maximum σ'_1 for a given σ'_3 decreases with θ, except at $\theta = 56^\circ$. Conversely, the lower values of unconfined compressive strength, defined by the constant term in the equations in Fig. 7, would correspond to $\theta = 0^\circ$, which seems unrealistic. This inconsistency could be related to an artefact due to the extrapolation of the linear adjustment at very low confining pressures.

5.2. Generalised H&B criterion

The non-linear strength criterion of H&B (Hoek, 1994; Hoek et al., 1995; Marinos and Hoek, 2000; Hoek and Brown, 2019) was used to analyse the results obtained from the tests (Fig. 8). The generalised H&B criterion is expressed as

$$\sigma'_1 = \sigma'_3 + \sigma_{ci}\left[m_b\frac{\sigma'_3}{\sigma_{ci}} + s\right]^a$$

$$m_b = m_i \cdot e^{\frac{GSI-100}{28-14D}}$$

$$s = e^{\frac{GSI-100}{9-3D}}$$

$$a = \frac{1}{2} + \frac{1}{6}\left[e^{\frac{-GSI}{15}} - e^{\frac{-20}{3}}\right]$$

where σ'_1 and σ'_3 are the major and minor principal effective stresses at failure, respectively; σ_{ci} is the uniaxial compressive strength; m_b, s, and a are rock mass material constants; GSI is the geological strength index; D is the disturbance factor (blast damage and/or stress relaxation); and m_i is a material constant that depends on the mechanical properties. GSI is denoted as 100 for intact rock, and the material constants become $m_b = m_i$, $s = 1$, and $a = 0.5$ when $D = 0$ (no disturbance).

Two approaches were used to define the strength criteria: (i) considering the fault gouge as *intact rock* and (ii) considering the fault gouge as *tectonised rockmass*. These approaches, were used to assess the suitability of the H&B criterion for the results of the laboratory tests and to determine which option offers better adjustments regarding the two extreme GSI values. Calculations for both options were conducted using the parameters of the H&B criterion updated by Hoek et al. (2002)

Table 2
Effective principal stresses σ'_3 and σ'_1 (kPa), deformation (%) and Skempton's A parameter at the *yield point* from the triaxial tests conducted at each orientation ($\theta = 0^\circ$, 37°, 44°, and 56°) and each confining pressure ($\sigma_3 = 50$, 150, and 300 kPa).

	$\theta = 0^\circ$				$\theta = 37^\circ$				$\theta = 44^\circ$				$\theta = 56^\circ$			
Test	σ'_3	σ'_1	Def (%)	SkmpA	σ'_3	σ'_1	Def (%)	Skmp A	σ'_3	σ'_1	Def (%)	Skmp A	σ'_3	σ'_1	Def (%)	Skmp A
50	29	162	3.1	0.21	69	280	2.0	−0.09	30	141	0.6	0.18	21	226	2.0	0.14
													71*	251*	4.0*	0.05*
150	119	461	1.3	0.09	167	579	3.0	−0.04	105	501	1.9	0.11	120	531	2.0	0.07
300	279	1155	2.5	0.02	217	680	3.0	0.18	203	544	3.9	0.28	216	709	2.0	0.17
													325*	949*	4.0*	0.08*

* Values from duplicated tests.

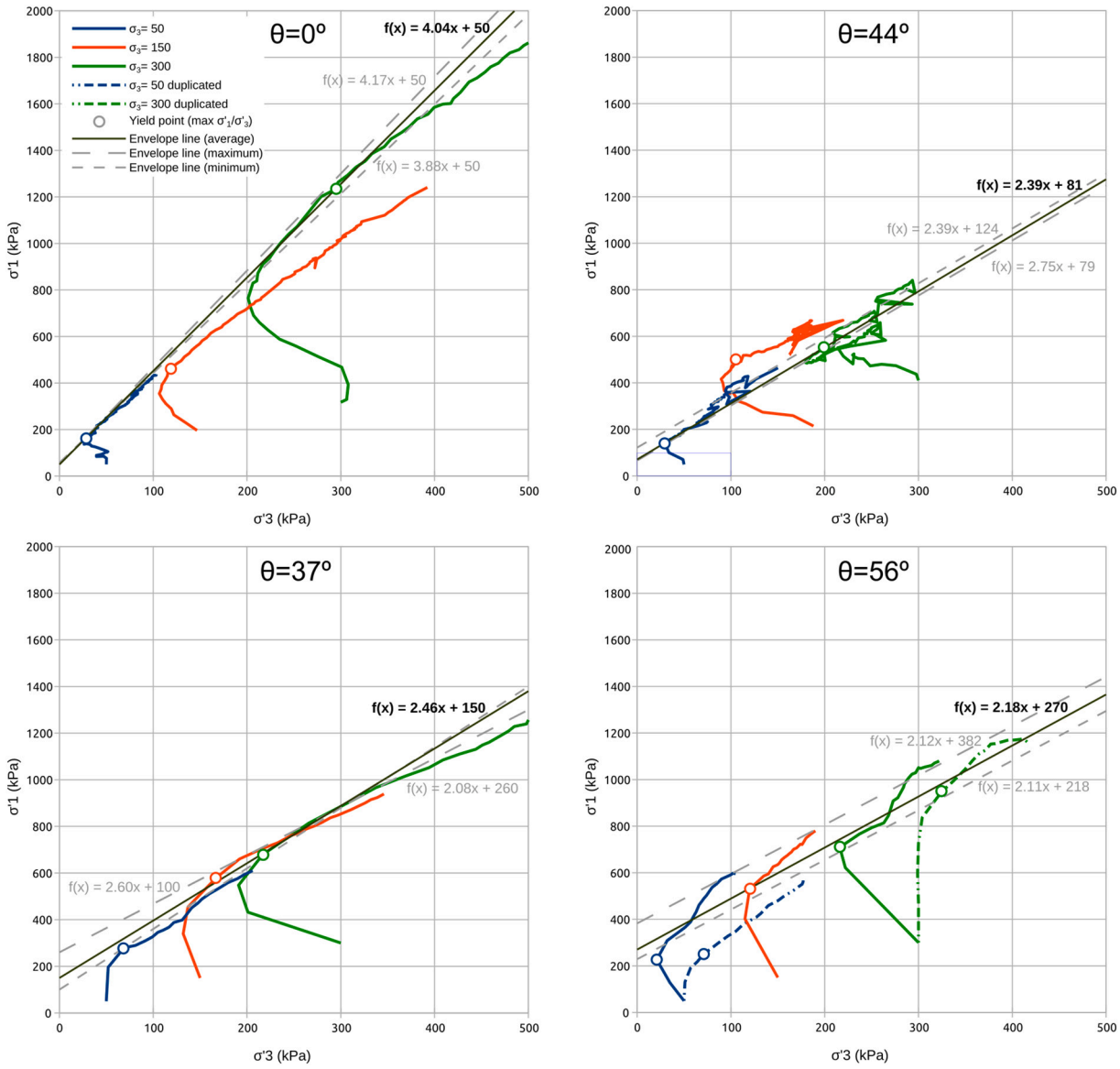

Fig. 6. σ'_1–σ'_3 paths at each orientation ($\theta = 0°$, 37°, 44°, and 56°) and confining pressures (σ_3 = 50, 150, and 300 kPa). Linear failure envelopes for every orientation are also displayed. Black line represents the average adjustment. Grey dashed lines correspond to extremely reliable adjustment (see Fig. 7A for an integrated comparison). The equations describing the envelopes are displayed.

(Tables 3A and 3B). The software RocData V3.015 (Rocscience Inc, 2005) was used for the calculation and regression fitting algorithms, after adjustments using the minimum residual sum of squares.

A GSI of 100 was adopted when the fault gouge was considered as *intact rock* (i) (Table 3A). The values for m_i and the unconfined compressive strength (σ_{ci}) were obtained by fitting the test results. The material constant m_i, calculated directly from the test data, yielded a value of 50 at all orientations, except for $\theta = 56°$, where m_i was equal to 7.9. Values of 50 for m_i are much greater than the values calculated for any other type of rock (Hoek, 2007), especially considering the low confining pressure (Wen et al., 2020). The number of test values for all orientations is well below the recommended number of five for estimating m_i (e.g. Hoek and Brown, 1997); the exception was for $\theta = 56°$ with four test values, which yielded the only realistic value. Therefore, the m_i estimated from tests with $\theta = 56°$ was considered to be representative of the material and m_i was assumed to be equal to eight for all the orientations. Unconfined tests were not performed in this study. The estimated σ_{ci} values, based on consideration of ratios at different orientations of principal stress values at yield point (Table 2), varied from 68 to 234 kPa. Depending on the orientation of the tectonic fabric, σ_{ci} decreases with θ, as expected, except at $\theta = 56°$, with a value of 140 kPa.

Regarding the strength criteria (Fig. 8A), the maximum σ'_1 for a given σ'_3 decreases with θ, except at $\theta = 56°$, which is opposite to what is suggested by the theory of anisotropy. The calculated values of tensile strength follow the same pattern, with values varying from 9 to 29 kPa reaching a value of 18 kPa at $\theta = 56°$ (Table 3A). Nevertheless, this tensile strength should be considered in terms of the relative variation that occurs as a result of the adjustment process, as the tensile strength is high at very small θ angles, with minimum values at $\theta = 90°$ (Vervoort et al., 2014).

A *triaxial anisotropy ratio* (R_1) is defined considering the relationship between the maximum (σ'_{1max}) and minimum (σ'_{1min}) values of resistance based on the estimated non-linear strength criteria within the range of the confining pressure used in the triaxial tests.

$$R_1 = \frac{\sigma'_{1max}}{\sigma'_{1min}}$$

Notably, R_1 would be equivalent to the anisotropy ratio R_c (sensu

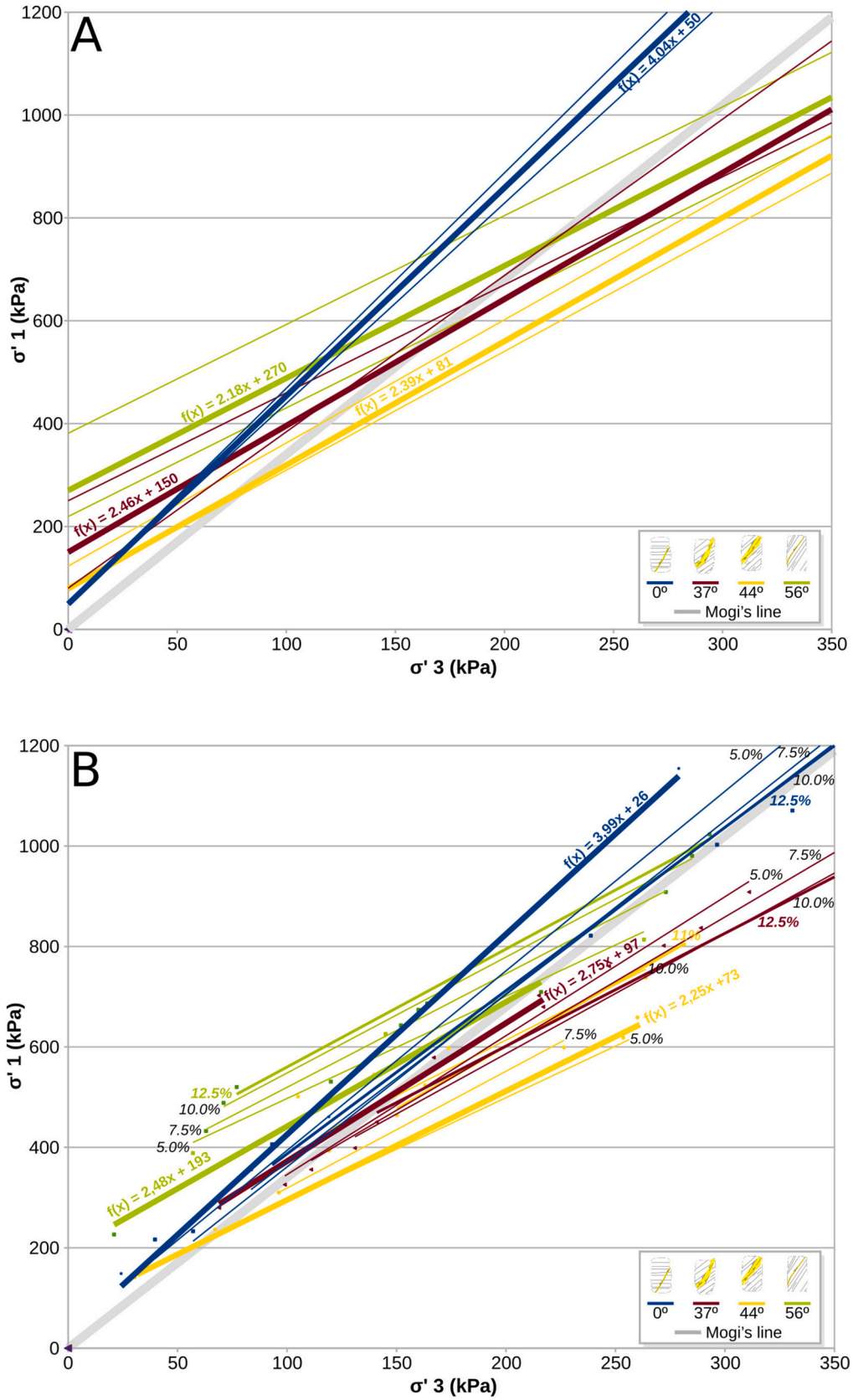

Fig. 7. Linear failure envelopes for every orientation with: A) the σ'_1-σ'_3 paths (see Fig. 6). Thick line represents the average value. Thin lines correspond to extremely reliable adjustment. B) Stress conditions for a given degree of deformation 5.0%, 7.5%, 10.0%, (thin lines), and 12.5% (medium line). Thick line shows maximum values of the σ'_1/σ'_3 relationship (yield point). The equations of the main envelopes are displayed for comparison. Note that the constant term in the equations would correspond the unconfined compressive strength in kPa.

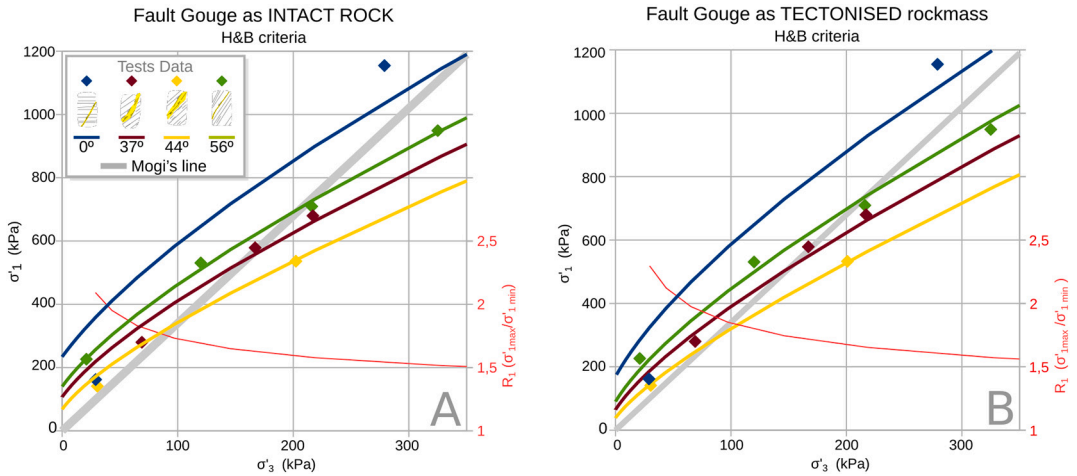

Fig. 8. Hoek and Brown strength criteria fitting the obtained data from the performed triaxial tests at each tectonic fabric orientation (θ = 0°, 37°, 44°, and 56°), while considering the fault gouge as: A) intact rock (Table 3A), and B) tectonised rockmass (Table 3B). Red line marks the triaxial anisotropy ratio (R_1). Mogi's line is also plotted ($\sigma'_1/\sigma'_3 = 3.4$) marking the brittle–ductile transition. (For interpretation of the references to colour in this figure legend, the reader is referred to the web version of this article.)

Table 3A
Parameters of the strength criteria obtained in this study considering the fault gouge as *intact rock*.

	Hoek&Brown classification		Hoek&Brown criterion			Intact rock parameters form H&B	
θ (°)	GSI	m_i	m_b	s	a	Tensile strength (−) (kPa)	Unconfined compressive strength (kPa)
0	100	8	8	1	0.50	29	234
37	100	8	8	1	0.50	13	107
44	100	8	8	1	0.50	9	68
56	100	8	8	1	0.50	18	140

Ramamurthy et al., 1993) when the confining pressure becomes null. R_1 has a maximum value of 2.10 at the lowest confining pressure, and decreases to 1.51 at the maximum confining pressure. This range is representative of the anisotropy at the confining pressure where the rock acts as brittle rock in the field where the H&B strength criterion is applicable (Hoek and Brown, 2019).

For estimating the strength criteria of the fault gouge when it is considered as a *tectonised rockmass* (ii), the fault gouge was considered the product of the intense and progressive comminution of the schists and phyllites in the metamorphic basement that constitute the protolith. We adopted a constant value of 20 MPa for σ_{ci} as a representative of the lowest values in this type of rock, while also considering the minimum resistance to failure that is favoured by the presence of cleavage (Hoek and Brown, 1997). A constant m_i of 3 was also considered to be related to the minimum value of m_i regarding the intrinsic anisotropy of the lithology of the protolith (Colak and Unlu, 2004). This m_i value is also consistent with the results obtained by Wen et al. (2020) for this type of rock regarding the confining pressure and the angle between the major principal stress and weakness plane. The disturbance factor (D) is assumed to be 0 because the drilling technique affects the rock only minimally beyond a negligible stress relaxation. The GSI values were then obtained by fitting the test data. The GSI was used as an indicator of the strength of the rockmass as associated with the direction of the tectonic fabric rather than as an indicator describing the degree of tectonisation that affects the entire rockmass, which would be unique following the standard use of GSI. This unique value of GSI could be assigned as 15 ± 5 based on the observation of the core as a field estimate. The obtained values of GSI (Table 3B) decreased with θ from 21 to 7, with a value of 14 recorded for θ = 56°. These values are consistent with those proposed by Marinos and Carter (2018) for a severe tectonisation process in a ductile protolith, as well as with those proposed by Habimana et al. (2002) for extremely tectonised phyllitic schists.

The strength criteria (Fig. 8B) again shows the maximum σ'_1 for a given σ'_3 to be decreasing with θ, except for θ = 56°. The calculated values of σ_{cm} for the rockmass varied from 39 to 142 kPa. The unconfined compressive strength, σ_{cm}, is maximum at θ = 0° and decreases with θ as expected, except at θ = 56°, which gives a value of 90 kPa. The tensile strength follows the same pattern, with a maximum value of 29 kPa at θ = 0° decreasing with θ to 9 kPa, except at θ = 56°, which gives a value of 18 kPa. In this case, the values for both parameters, unconfined compressive strength and tensile strength, are around 60% of those estimated when considering the fault gouge as an intact rock (Tables 3A and 3B). R_1 has a maximum value of 2.30 at the lowest confining pressure, which decreases rapidly to stabilise within the range of 1.70 to 1.57.

6. Mineralogy and microstructure of the fault gouge

X-ray diffraction (XRD) analyses of the powders (bulk-rock samples) from both the protolith and the fault gouge show that all samples contain a high amount of K and Na micas (muscovite/paragonite) and quartz (Fig. 9). A small amount of carbonate (calcite/dolomite or

Table 3B
Parameters of the strength criteria obtained in this study considering the fault gouge as *tectonised rockmass*.

	Hoek&Brown classification			Hoek&Brown criterion			Rockmass parameters from H&B	
θ (°)	Intact unconfined compressive strength (kPa)	GSI	m_i	m_b	s	a	Tensile strength (−) (kPa)	Unconfined compressive strength (kPa)
0	20,000	21	3	0.179	0.0002	0.541	17	173
37	20,000	11	3	0.125	0.0001	0.580	8	65
44	20,000	7	3	0.108	0.00003	0.604	6	39
56	20,000	14	3	0.139	0.0001	0.565	10	90

ankerite), chlorite, and Fe-oxides are also present in some of the samples. The high amounts of K- and Na- micas in these rocks are consistent with the data obtained in previous studies from the Alpujárride Complex (Abad et al., 2003; Abad et al., 2019).

Clay minerals that are determined to be present in all the gouge samples are represented by illite (60–95%); followed by a variable amount of paragonite (12–25%) and a lesser amount of kaolinite (5–10%). A small amount of Ca-smectite was identified in some samples using SEM with typical cornflake microfabric (Tsige et al., 2017). Little or no variation is observed in the mineralogical composition of the gouge compared to the adjacent protolith, indicating that few fault-related mineralogical or chemical processes occurred during deformation. Both the micaceous illite and paragonite clays result from the gradual mechanical breakdown, fragmentation, and commination of previous micas through frictional sliding (Tsige et al., 2017; Rodríguez-Escudero et al., 2020).

From a microstructural point of view, despite the high degree of deformation that has developed a marked macroscale tectonic fabric along the fault plane, the fault gouge presents an important heterogynous internal microfabric or arrangement that can control the mechanical behaviour of the fault rock. Fig. 10A and B show microphotographs of the protolith and the fault gauge observed via optical microscopy of the polished thin sections. The original features of the protolith (Fig. 10A), with well-developed schistosity, are offset and replaced by a highly fragmented and comminuted rock that produces a very fine grained matrix-type gouge with large heterometric clasts embedded within (Fig. 10B).

The structure of the fine-grained foliated gouge that is parallel to the foliation (Fig. 10C) seen under SEM is characterised by highly deformed morphological features with the typical smooth and polished surfaces and traces of slickensides that includes features such as lineations, irregularly shaped grooves, and curved fractures. The microstructure on the perpendicular surface is characterised by a continuous and anastomosing matrix that in which small-scale ridge and grove like structures are developed (Fig. 10D). These structures are intercepted by very thin (less than a micron in width) and discontinuous secondary shear planes (white arrows in Fig. 10D).

The alignment of the clay minerals can be observed in close-up SEM images that were obtained at a higher magnification, with formations of clearly scaly type clay fabric that are mostly wrapped around the observed porphyroclasts (Fig. 10E). These form a network a of minor shear planes (S planes), that are identified by small clay packets with a strongly preferred orientation, forming typical wavy and anastomosing features with lens-shaped separation of the layers (Fig. 10F). The relative orientation of the clay packets is variable, especially as they commonly intersect at low angles with other packets that kink and bend

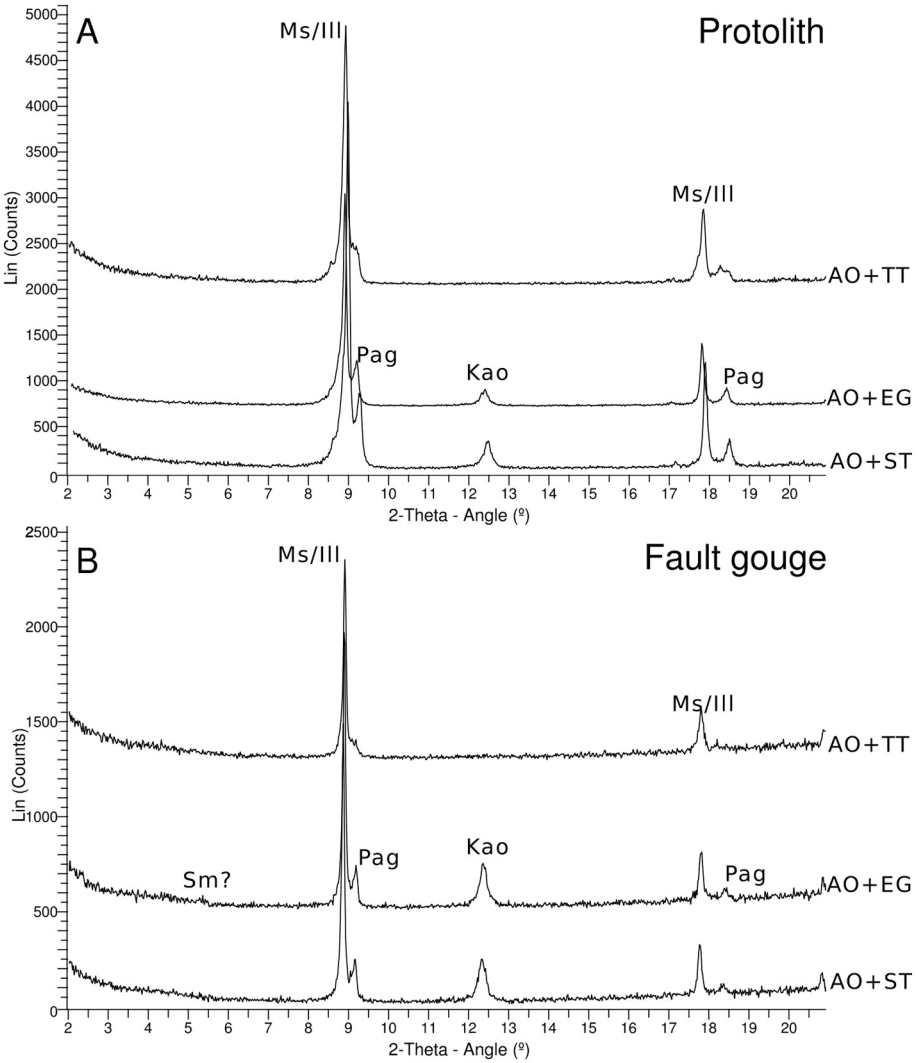

Fig. 9. Representative XRD pattern of clay fractions <2 μm of A) the protolith collected at a depth of 20 m from borehole AMF-1, and B) the fault gouge taken at a depth of 144 m from borehole AMF-1. AO + ST: oriented aggregate; AO + EG: ethylene glycolated; AO + TT: heated at 550 °C; Ms./Ill = Muscovite/Illite; Pag = Paragonite; Kao = Kaolinite; and Sm = Smectite.

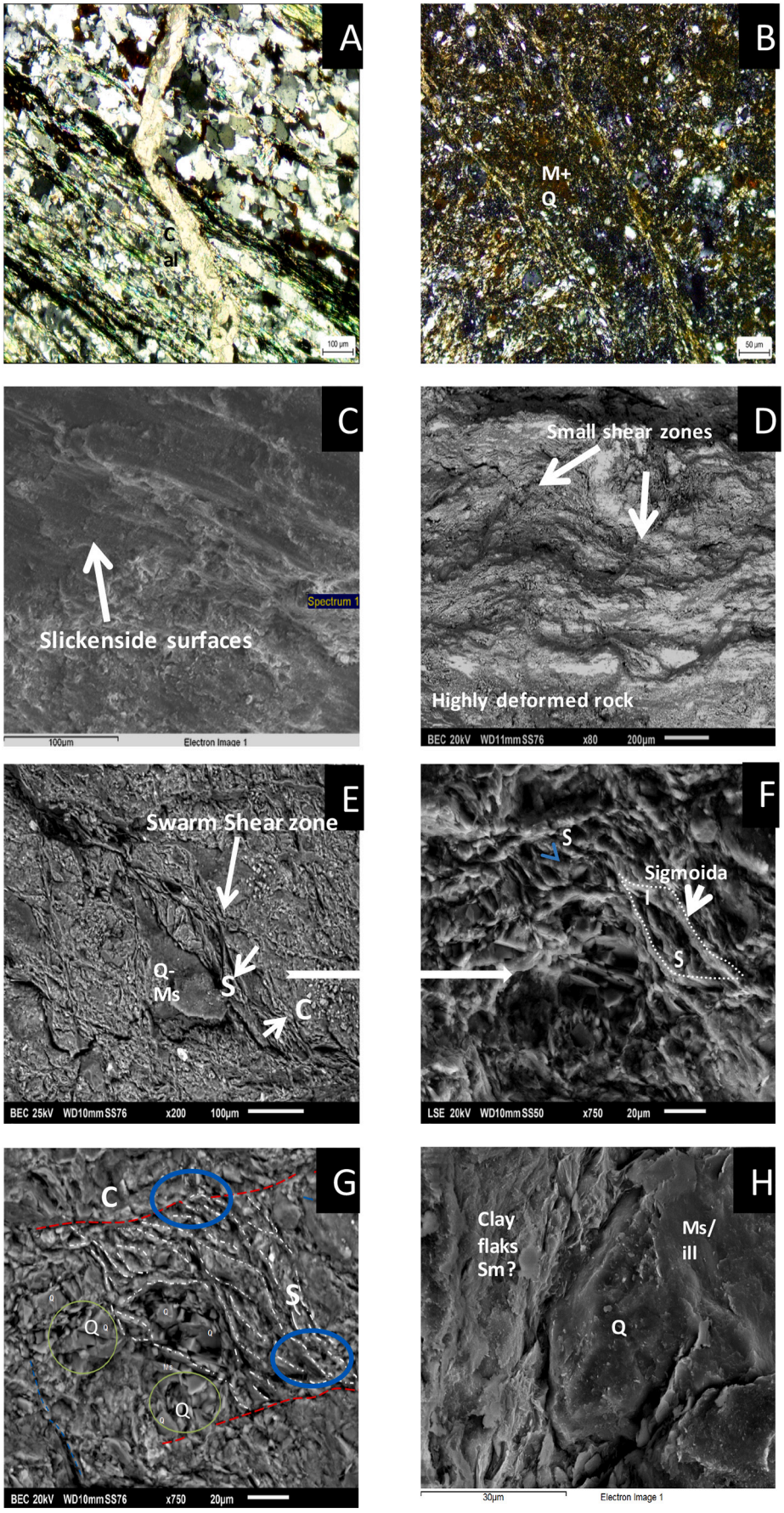

Fig. 10. Microphotographs of the *meso* and microstructure of the fault gouge in the AMF. (A) Images of thin sections observed under optical microscopy of the hanging wall protolith (Alpujárride Schists) with well-developed schistosity that is sometimes intercepted by calcite veins. (B) The fault gouge, highly fragmented and crushed rock where the original texture is overprinted by heterometric clasts embedded in a fine-grained detrital origin matrix. Clasts embedded in the fault gouge matrix are predominantly comminuted or pulverized quartz and mica grains, with fragments of schist and some Fe-oxides. (C) SEM image of the fault gouge at a larger scale seen parallel to the tectonic foliation with polished like surface (slickensides) giving a ridge-and-grove feature. The polished surface is due to the strong reorientation of illite/mica. (D) Photomicrograph of typical anastomosing microstructure of the gouge with very thin shear planes (white arrows). (E) Close-up observation of the microstructure of the gouge hosting multiple "shear planes" that form a complex network in which packets of oriented phyllosilicates are truncated (green circles, in G) with another group to form the typical scaly microfabric. (F) Sigmoidal structure of the clay packets separated by oval shape pores. (G) Image shows a S-C′ like structure. (H) Phyllosilicates mantling the large quartz clasts seen parallel to tectonic foliation. D–G are taken perpendicular to tectonic foliation. (For interpretation of the references to colour in this figure legend, the reader is referred to the web version of this article.)

the clay (marked by white lines in Fig. 10F and G) and irregularly distributed small and large quartz crystals. The preferred orientations of the clays are also truncated by thin localised shear zones (Fig. 10G, red lines, C′ planes), which can be identified by a strongly preference in the orientation of the mica-like platy clay minerals. Rotations at the edge of the clay mineral flakes (marked by the green circle in Fig. 10G) along the plane direction are observed in the localised shear zone, giving an S-C′ like structure. The continuous thin clay packets that are anastomosed and truncated by the thin planes can severely exaggerate the small-scale surface roughness that ranges from a marked asymmetrical roughness to polished slickenside surfaces depending on the direction of observation. The clay packets occasionally cover and mantle (Fig. 10G and H) rigid quartz crystals, where a ridge- and grove-like structure can be developed by the increasing surface roughness.

7. Discussion

We consider that consistent results are observed for the H&B strength criteria obtained by the two approaches used for the analysis of the fault gouge. These results are also consistent with those obtained using the linear regressions in Section 5.1. However, the results obtained from the H&B strength criteria fit the test data better showing more realistic values, especially at a lower confining pressure. The estimation of the strength criteria following hypothesis (ii), which considers the fault gouge as a *tectonised rockmass*, has the advantage of using GSI, which is a quick and simple index to obtain. Nevertheless, a combination of good field observation and laboratory tests is essential for correctly assessing the rockmass properties.

If we exclude the results obtained with the orientation of $\theta = 56°$, the H&B strength criteria achieved by the two approaches satisfy the theory of strength anisotropy. The maximum compressive strength values occur when the weakness planes are perpendicular to the axial load, while failure occurs through the matrix bypassing the weakness planes. The resistance decreases when the weakness planes become oriented to favour failure, with minimum values at $\theta = 44°$. The R_1 was estimated to have a maximum value of 2.55–2.30 at the lowest confining pressure, with a mean range of 1.70–1.51. These values could be slightly higher if we assume that lower minimum values of resistance are expected to be reached with values of θ that are close to 60°, according to the theory of anisotropy. Thus, we can conclude that the fault gouge exhibits low to medium anisotropic behaviour following the classification proposed by Ramamurthy et al. (1993).

Nevertheless, the results from $\theta = 56°$ do not fit the theory, since the strength at this orientation is greater than that at any of the other intermediate orientations of the weakness planes, although tit is markedly less than the strength at $\theta = 0^0$ (see Fig. 8). Such an anomalous result could be mechanically explained by the tectonic fabric of the fault gouge. As described above, the main planes that are observed in the specimens correspond to the C′ planes, parallel planes with the greatest persistence. S planes link the C′ planes with a sigmoidal shape (Fig. 2A). This tectonic fabric is observed at macro, *meso*, and micro scales, with C′ and S planes defined by the reorientation of platy minerals (phyllosilicates) (Fig. 10).

In terms of resistance, the C′ planes are the weakest and most continuous of the tested specimens, but they are far from being completely flat. C′ planes are noticeably rough asymmetrically, with the direction of the roughness depending on the direction of the plane even at microscales (Fig. 10C). Fig. 11 shows a C′ plane surface split from one of the drill cores. A 3D digital model of the split surface on both sides was made using PhotoScan v. 1.2.5 (AgiSoft, 2016) and QGIS v3.16 (QGIS.org, 2021) to analyse the variation in the roughness with direction on the mesoscale.

Mesotopographic profiles were made every 15° (the rake of the line within the plane was taken as reference for the orientation, with 0° being along the horizontal line within the plane to the left). Two different reference points were taken at both sides of the split surface to evaluate the variations along the plane. Note that the orientation of the profiles is symmetrically opposed at the upper and lower sides. The obtained profiles (Fig. 12) indicate that the variation in roughness depends on the orientation.

The *smoothness* factor (sensu Palmström, 2001), which attempts to quantify the roughness or asperities for a given rock plane, was calculated by dividing the amplitude of each profile by its length (Fig. 12). The orientations with a rake of 0° and 15° show the minimum smoothness values (approximately 4–7%), whereas a rake of −75° shows the maximum values (approximately 17–19%). Nonetheless, these smoothness factors must be taken as relative rather than absolute values because the actual persistence of the C′ planes is diminished by the intercept of secondary shear planes (S plane) developing ridge- and groove-like structures (see Section 6, Fig. 10D). The roughness implies anisotropy in terms of the resistance within the plane, which not only depends on the orientation of the weakness plane with respect to the applied load but is also associated with the orientation of the load with respect to the roughness of the plane.

Specimens where $\theta = 37°$ and 44° are oriented more favourably with respect to the direction of the smoothest profiles (Fig. 13).

These specimens have a noticeable angle (34° and 54°, respectively) between the line of maximum dip within the failure plane and the profile with the maximum roughness (Table 1). On the contrary, in specimens with $\theta = 56°$, the line of maximum dip within the failure plane is oriented almost along the roughest profiles (with a difference of only 9°, Table 1), offering greater resistance. This explanation could be supported by the anomalously high value of 14 for GSI (see Table 3B). This fact suggests that the GSI is sensitive not only to the degree of tectonisation, but also to the orientation of the load with respect to the weakness plane, and even to the direction of the roughness profiles within the weak planes.

Regarding the curves for the strength criteria obtained for $\theta = 0°$ and $\theta = 56°$ (Fig. 8B), the R_1 calculated for all the performed triaxial tests was as low as 1.3–1.1. Moreover, as the strength for $\theta = 56°$ may be even higher if the plane orientation favours the displacement of the failure perfectly along the maximum roughness (rake −75°), the R_1 could decrease to approximately 1, producing apparently perfect isotropic behaviour for the strength within the gouge. On the contrary, if the displacement occurs along the minimum roughness (rake between −15° and 15°) for a θ of approximately 60°, the resistance would be the lowest possible for the gouge. In this case, R_1 may reach maximum values greater than 2.5.

There is also a secondary factor related to the asymmetry in the roughness of every profile owing to the direction of displacement induced by the test (Fig. 12). This could also imply the presence of steeper up-riding irregularities (mechanical asperities) on the shear surface that are flatter in the natural tectonic direction of displacement than in the opposite direction. This asymmetry should be controlled by the tails of the sigmoids related to the S planes. Such a microfabric feature also implies anisotropy in terms of resistance. This effect has been widely described in terms of pre-existing cracks (Coulson, 1972; Bock, 1979), but the asymmetry in this case is controlled by the geometry of the tectonic fabric (Rodríguez-Escudero, 2017) (Fig. 14).

Fig. 14 shows the results of ring shear tests that were designed by Rodríguez-Escudero (2017) to investigate the role of the microstructure on the frictional behaviour of gouges in normal fault zones that have been reactivated as reverse faults, or vice versa. Gouge and schist samples from the AMF-1 borehole were studied for this purpose. The remoulded samples of gouges were initially sheared to establish an initial normal microstructure, after which the experiment was changed to a direction contrary to the initial direction of the shear (see Rodríguez-Escudero, 2017 for details of the experimental environment). Samples with reverse fabric (dashed lines in Fig. 14) show a higher friction peak than homologous samples with normal fabric (solid lines in Fig. 14), which was interpreted by Rodríguez-Escudero (2017) as being mostly controlled by the microstructure, which must be removed before

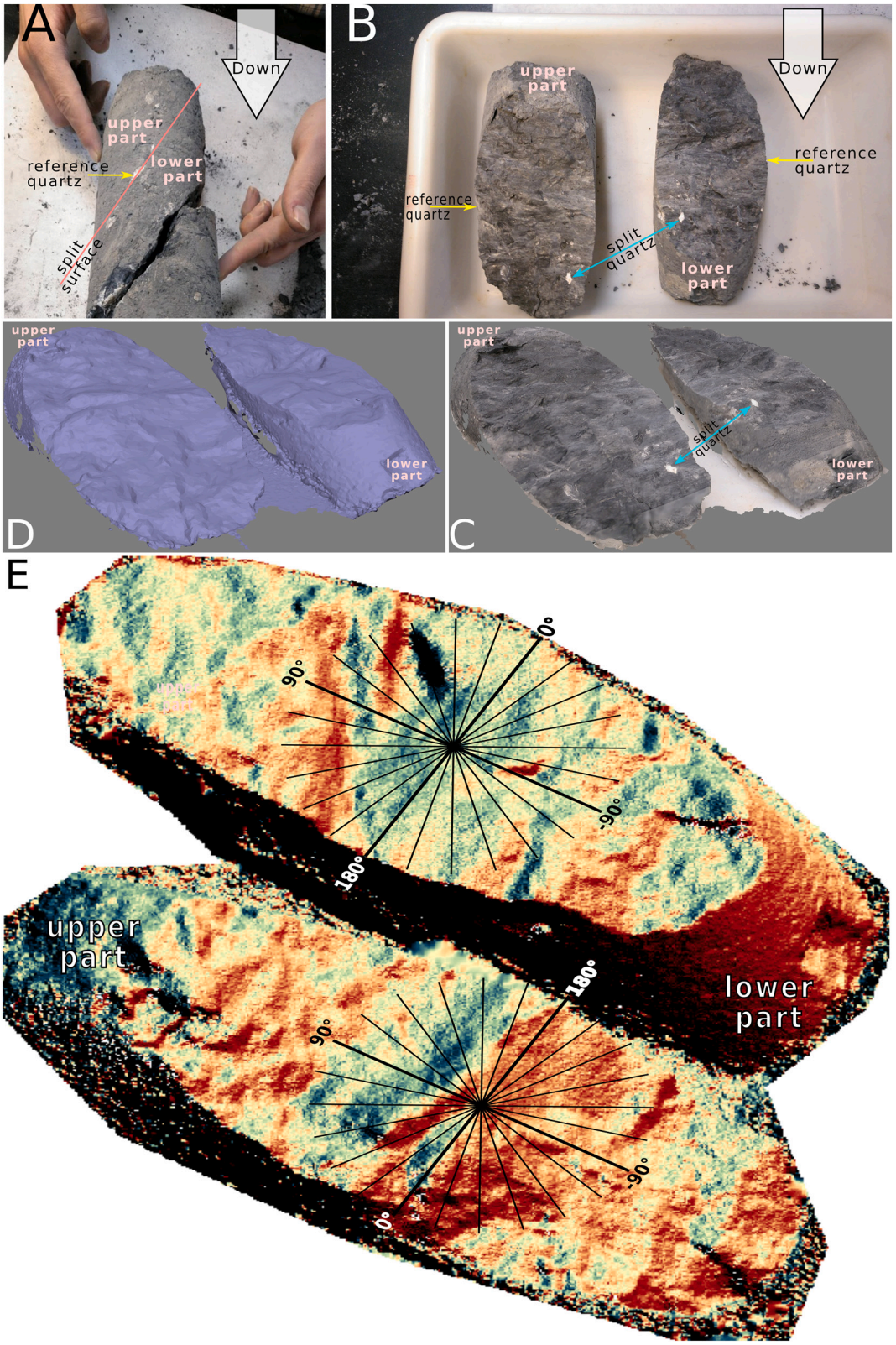

Fig. 11. Split C′ plane in a core sample (from AMF-1 borehole at 155 m depth). A) Core sample in which the split surface is located. B) Both sides of the split surface in the core sample. C) 3D digital model of the split surface. D) 3D oblique view of the digital shadow model of the split surface. E) Digital model of the split surface coloured by surface orientation. Radial lines correspond to mesotopographic profiles of Fig. 12.

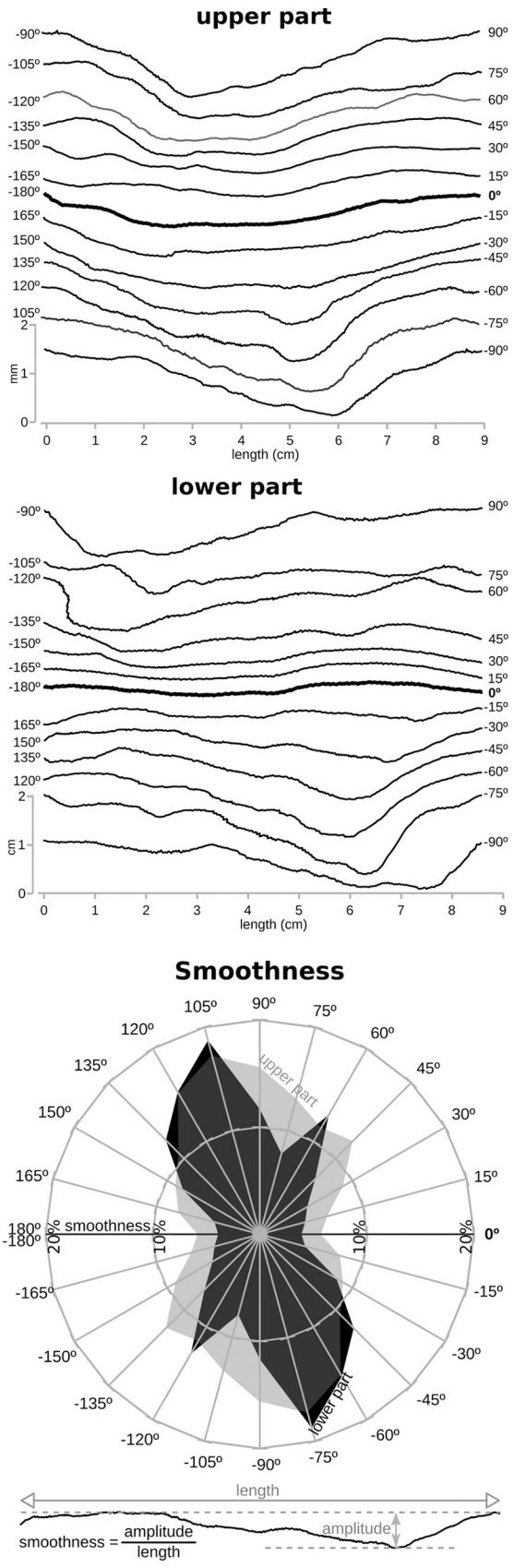

Fig. 12. Mesotopographic profiles of the upper and lower part of the C′ plane split surface. Location and orientation of the profiles shown in Fig. 11E. Distribution of the smoothness with the orientation of the plane is also displayed.

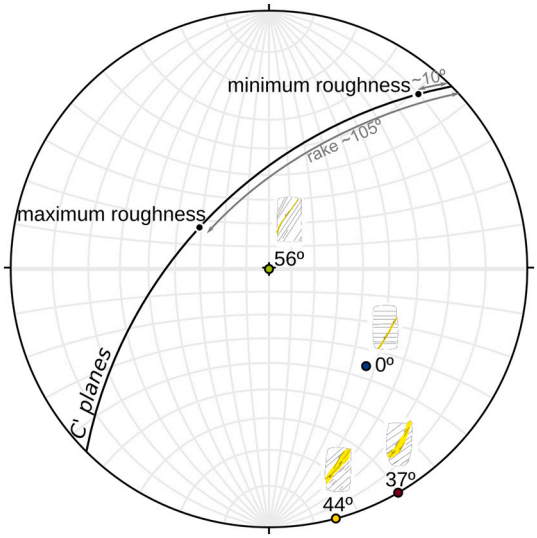

Fig. 13. Stereographic projection (equal angle, lower hemisphere) of the C′ planes displaying the maximum and minimum roughness orientations of surfaces together with their rake. Orientations of the axial load of the tested specimens are also displayed (see values on Table 1).

being reorganised by the new shear direction. The asymmetry in the roughness geometry (as described in this study for C′-planes) along the possible reactivated planes that are related to the initial normal fabric could offer a higher strength. This effect evokes a dilatational phenomenon at low confining pressures under which the triaxial tests were performed, as is observed in tests with $\theta = 56^{\circ}$ under the lowest confining pressure of 50 kPa (Fig. 5 B). The anomalously high values of σ_{cm} and tensile strength obtained for that orientation could also be explained by dilatancy.

8. Conclusions

The results of consolidated-undrained (CU) triaxial tests performed under low confining pressure (<300 kPa) on several sets of clay-rich fault gouges that were carved with different orientations of the tectonic fabric suggest that the strength of the foliated gouge is controlled not only by the orientation of the load with respect to the weakness planes but also by the roughness within the weak planes themselves. Such roughness is defined by the original gouge microstructure, which is characterised by a strong reorientation of the clays in an S-C′-like tectonic fabric. The strength of the gouge shows medium to low anisotropic behaviour with a ratio between the maximum and minimum values of resistance for a given confined pressure (triaxial anisotropy ratio, R_1) that ranges from 1.5 to 2.5. Nevertheless, the gouge could be considered as isotropic (R_1 close to 1) if failure occurs along the maximum roughness profiles within the weakness planes.

The strength results show that the studied clay-rich gouge behaves as hard soil or very soft rock with a brittle-ductile transition at low confining pressures such as those at which our triaxial tests were performed. The failure in each test is determined by the maximum value of the ratio σ_1/σ_3, which marks the yield point, that is, when the elastic deformation becomes plastic. These facts allowed us to adjust the non-linear Hoek and Brown strength criterion by considering two approaches: (i) considering the fault gouges as *intact rock*, and (ii) considering the fault gouge as *tectonised rockmass*. In the former case, a value of $m_i = 8$ was used, derived from the most complete data set, with assigned unconfined compressive strength values for other fabric orientations. In the latter individual values of GSI were assigned for each fabric orientation rather than using a uniform value for the overall tectonised rock mass. GSI was not only able to consider the orientation of the load with respect to the weakness plane, while considering the

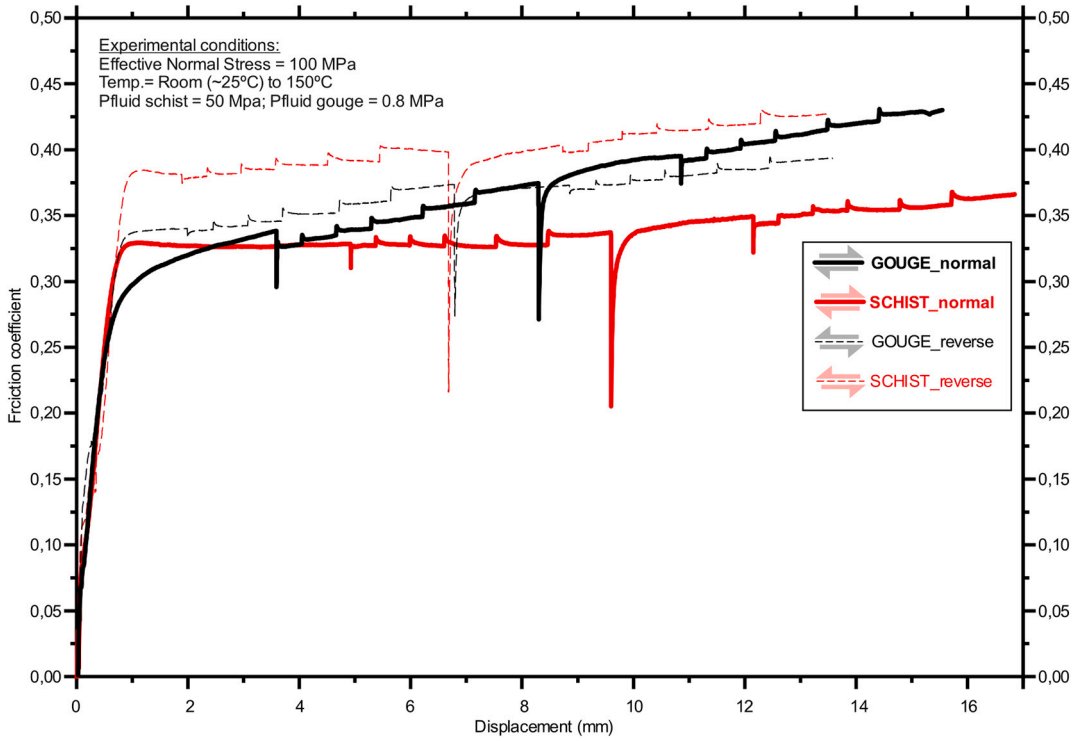

Fig. 14. Evolution of the coefficient of friction (shear stress/normal stress, ignoring cohesion) with displacement for four ring shear tests performed by Rodríguez-Escudero (2017) on core samples of gouge (black lines; 126 m depth) and schist (red lines; 34 m depth) from the Alhama de Murcia Fault-1 Borehole (Martínez-Díaz et al., 2016). (For interpretation of the references to colour in this figure legend, the reader is referred to the web version of this article.)

direction of the roughness profile within the weak planes themselves.

This work contributes to the knowledge of anisotropic behaviour of the brittle fault zone and provides guidelines for appropriate evaluation of the strength in future projects involving shallow underground excavation, engineering slope stability, mining, and major foundation engineering (e.g., dams). This study also provides insights on the geomechanical properties of gouges that control the seismogenic behaviour of active faults.

Declaration of Competing Interest

The authors declare that they have no known competing financial interests or personal relationships that could have appeared to influence the work reported in this paper.

Acknowledgements

This research was supported by the "QUAKESTEP" project (CGL2017–83931-C3-1-P) funded by the Spanish Ministry of Science, Innovation and Universities. J.L. Sánchez-Roldán received a predoctoral research grant (FPI) supported by the same project. The authors would like to acknowledge the comments and suggestions of the three anonymous reviewers.

Appendix A. Supplementary data

Supplementary data to this article can be found online at https://doi.org/10.1016/j.enggeo.2021.106186.

References

Abad, I., Nieto, F., Peacor, D.R., Velilla, N., 2003. Prograde and retrograde diagenetic and metamorphic evolution in metapelitic rocks of Sierra Espuña (Spain). Clay Miner. 38, 1–23.

Abad, I., Jiménez-Millán, J., Sánchez-Roa, C., Nieto, F., Velilla, N., 2019. Neo-crystallization of clay minerals in the Alhama de Murcia Fault (SE Spain): implications for fault mechanics. Clay Miner. 1–34. https://doi.org/10.1180/clm.2019.2.

AgiSoft, 2016. AgiSoft PhotoScan Professional (Version 1.2.6) (Software).

ASTM D 4767-95, 1995. Standard Test Method for Consolidated Undrained Triaxial Compression Test for Cohesive Soils. American Society For Testing And Materials (11 pp.).

Attewell, P., Sandford, M., 1974. Intrinsic shear strength of a brittle, anisotropic rock—I. Experimental and mechanical interpretation. Int. J. Rock Mech. Min. Sci. Geomech. Abstr. 11, 423–430. https://doi.org/10.1016/0148-9062(74)90453-7.

Bao, H., Qi, Q., Lan, H., Yan, C., Feng, L., Xu, J., Yin, P., Peng, J., 2020. Sliding mechanical properties of fault gouge studied from ring shear test-based microscopic morphology characterization. Eng. Geol. 279, 105879. https://doi.org/10.1016/j.enggeo.2020.105879.

Bieniawski, Z.T., 1967. Mechanism of brittle fracture of rock. Int. J. Rock Mech. Min. Sci. Geomech. Abstr. 4 (4), 395–406. https://doi.org/10.1016/0148-9062(67)90030-7.

Biscaye, P.E., 1965. Mineralogy and sedimentation of recent deep-sea clay in the Atlantic Ocean and adjacent seas and oceans. Geol. Soc. Am. Bull. 76, 803–832.

Bock, H., 1979. A simple failure criterion for rough joints and compound shear surfaces. Eng. Geol. 14, 241–254. https://doi.org/10.1016/0013-7952(79)90066-8.

Colak, K., Unlu, T., 2004. Effect of transverse anisotropy on the Hoek–Brown strength parameter 'm_i' for intact rocks. Int. J. Rock Mech. Min. Sci. 41, 1045–1052. https://doi.org/10.1016/j.ijrmms.2004.04.004.

Coulson, J.H., 1972. Shear strength of flat surfaces. In: Rock. Proc. 13th Syrup. Rock Mech. ASCE, pp. 77–105.

Habimana, J., Labiouse, V., Descoeudres, F., 2002. Geomechanical characterisation of cataclastic rocks: experience from the Cleuson-Dixence project. Int. J. Rock Mech. Min. Sci. 39, 677–693. https://doi.org/10.1016/S1365-1609(02)00042-4.

Hoek, E., 1994. Strength of rock and rock masses. ISRM New J. 2 (2), 4–16.

Hoek, E., 2007. Practical Rock Engineering. http://www.rocscience.com (Accessed 7 November 2019).

Hoek, E., Brown, E.T., 1980. Underground Excavations in Rock. Inst. Min Metall, London.

Hoek, E., Brown, E.T., 1997. Practical estimates of rock mass strength. Int. J. Rock Mech. Min. Sci. Geomech. Abstr. (34-8), 1165–1186.

Hoek, E., Brown, E.T., 2019. The Hoek-Brown failure criterion and GSI – 2018 edition. J. Rock Mech. Geotech. Eng. 11, 445–463. https://doi.org/10.1016/j.jrmge.2018.08.001.

Hoek, E., Kaiser, P.K., Bawden, W.F., 1995. Support of Underground Excavations in Hard Rock. Balkema, Rotterdam, p. 215.

Hoek, E., Carranza Torres, C., Corkum, B., 2002. Hoek-Brown criterion – 2002 edition. In: Hammah, R., Bawden, W., Curran, J., Telesnicki, M. (Eds.), Mining and Tunnelling Innovation and Opportunity, Proceedings of the 5th North American

Rock Mechanics Symposium and 17th Tunnelling Association of Canada Conference. University of Toronto, Toronto, Canada, pp. 267–273.
Ismael, M., Konietzky, H., 2019. Constitutive model for inherent anisotropic rocks: Ubiquitous joint model based on the Hoek-Brown failure criterion. Comput. Geotech. 105, 99–109. https://doi.org/10.1016/j.compgeo.2018.09.016.
Julià, R., Santanach, P., 1998. Banded structures in gouge. In: Snoke, A.W., Tullis, J., Todd, V.R. (Eds.), Fault-Related Rocks, pp. 56–57.
Kang, Y., Liu, Q., Xi, H., Gong, G., 2018. Improved compound support system for coal mine tunnels in densely faulted zones: a case study of china's Huainan coal field. Eng. Geol. 240, 10–20.
Liu, Q., Button, E., Klima, K., 2007. Investigation for probabilistic prediction of shearstrength properties of clay-rich fault gouge in the Austrian alps. Eng. Geol. 94, 103–121. https://doi.org/10.1016/j.enggeo.2007.08.001.
López Sopeña, F., 2005. In: ADIF (Ed.), Perfil geológico del túnel de Guadarrama. Estudios de caracterización de fallas: La Umbría. Túnel de Guadarrama, Madrid, pp. 147–189.
Marinos, P., Hoek, E., 2000. GSI: a geologically friendly tool for rock mass strength estimation. In: GeoEng2000. Melbourne.
Marinos, V., Carter, T.G., 2018. Maintaining geological reality in application of GSI for design of engineering structures in rock. Eng. Geol. 239, 282–297. https://doi.org/10.1016/j.enggeo.2018.03.022.
Martínez-Díaz, J.J., Bejar-Pizarro, M., Álvarez-Gómez, J.A., Mancilla, F.L., Stich, D., Herrera, G., Morales, J., 2012. Tectonic and seismic implications of an intersegment rupture. The damaging May 11th 2011 Mw 5.2 Lorca, Spain, earthquake, Betic Cordillera, Spain. Tectonophysics 546–547, 28–37. https://doi.org/10.1016/j.tecto.2012.04.010.
Martínez-Díaz, J.J., Insua-Arévalo, J.M., Tsige, M., Rodríguez-Escudero, E., Alonso-Henar, J., Crespo, J., Jiménez-Molina, D., Moratalla, J.M., Rodríguez-Peces, M.J., Álvarez-Gómez, J.A., Pérez-López, R., Jurado, M.J., Alvaro, M., Capote, R., 2016. FAM-1 Borehole: first results from the scientific drilling of the Alhama de Murcia Fault, Betic Cordillera, Spain. GeoTemas 16 (2), 579–582.
Moore, D.M., Reynolds, R.C., 1997. X-Ray Diffraction and the Identification and Analysis of Clay Minerals, 2nd ed. Oxford University Press, New York. (378 pp.).
Morrow, C.A., Shi, L.Q., Byerlee, J.D., Sammis, C.G., 1982. Strain hardening and strength of clay-rich fault gouges. J. Geophys. Res. 87 (B8), 6771–6780. https://doi.org/10.1029/JB087iB08p06771.
Niemeijer, A.R., Vissers, R.L., 2014. Earthquake rupture propagation inferred from the spatial distribution of fault rock frictional properties. Earth Planet. Sci. Lett. 396, 154–164. https://doi.org/10.1016/j.epsl.2014.04.010.
Palmström, A., 2001. Measurement and characterization of rock mass jointing. In: Sharma, V.M., Saxena, K.R. (Eds.), In-situ Characterization of Rocks. A. A. Balkema publishers, pp. 49–97.
QGIS.org, 2021. QGIS Geographic Information System. QGIS Association. http://www.qgis.org.
Ramamurthy, T., Venkatappa, R.G., Singh, J., 1993. Engineering behaviour of phyllites. Eng. Geol. 33, 209–225. https://doi.org/10.1016/0013-7952(93)90059-L.
Rocscience Inc, 2005. RocData, Version 3,015, Computer Software. Rocscience Inc, Toronto.
Rodríguez-Escudero, E., 2017. Implicaciones de la estructura interna de una zona de falla activa en la génesis de terremotos. PhD Thesis. Universidad Autónoma de Madrid (304 pp.).
Rodríguez-Escudero, E., Niemeijer, A., Martínez-Díaz, J.J., Giner-Robles, J.L., Tsige, M., Insua-Arévalo, J.M., Cuevas-Rodríguez, J., 2018. In: Canora, C., Martín, F., Masana, E., Pérez, R., Ortuño, M. (Eds.), Propiedades mineralógicas y friccionales de la gouge de la Falla de Alhama de Murcia (SE España): implicaciones sismogénicas. Tercera reunión ibérica sobre fallas activas y paleosismología, Alicante (España), pp. 191–194.
Rodríguez-Escudero, E., Martínez-Díaz, J.J., Giner-Robles, J.L., Tsige, M., Cuevas-Rodríguez, J., 2020. Pulverized quartz clasts in gouge of the Alhama de Murcia fault (Spain): evidence for coseismic clast pulverization in a matrix deformed by frictional sliding. Geology 48, 283–287. https://doi.org/10.1130/G47007.1.
Rutter, E.H., Maddock, R.H., Hall, S.H., White, S.H., 1986. Comparative microstructures of natural and experimentally produced clay-bearing fault gouges. In: Wang, C. (Ed.), Internal Structure of Fault Zones: Pure and Applied Geophysics, 124, pp. 3–30. https://doi.org/10.1007/BF00875717.
Saroglou, H., Tsiambaos, G., 2008. A modified Hoek-Brown failure criterion for anisotropic intact rock. Int. J. Rock Mech. Min. Sci. 45, 223–234. https://doi.org/10.1016/j.ijrmms.2007.05.004.
Sausgruber, T., Brandner, R., 2003. The relevance of brittle fault zones in tunnel construction - lower Inn Valley feeder line North of the Brenner Base Tunnel, Tyrol. Austria. Aust. J. Ear. Sci. 94, 157–172.
Schubert, W., Fasching, A., Goricki, A., 2006. Tunnelling in fault zones – state of the art. In: Lee, In-Mo, Yoo, Chungsik, You, Kwang-Ho (Eds.), Safety in Underground Space, vol. 21. Tunnelling and Underground Space Technology (abstract 376–377).
Scott, D.R., Lockner, D.A., Byerlee, J.D., 1994. Triaxial testing of Lopez Fault gouge at 150 MPa mean effective stress. PAGEOPH 142, 749–775. https://doi.org/10.1007/BF00876063.
Skempton, A.W., 1954. The pore-pressure coefficients A and B. Géotechnique 4, 143–147.
Tsige, M., Insua-Arévalo, J.M., Martínez-Díaz, J.J., Rodríguez-Escudero, E., Rodríguez-Soto, P., Crespo, E., Mata, P., 2017. Microfabric, Mineralogical and Geomechanical Characterization of Clay Rich Fault Gouge from AMF (Murcia, Southeast Spain). Scientific research Abstract, VII International Clay Conference, Granada, Spain.
Vervoort, A., Min, K., Konietzky, H., Cho, J., Debecker, B., Dinh, Q., Frühwirt, T., Tavallali, A., 2014. Failure of transversely isotropic rock under Brazilian test conditions. Int. J. Rock Mech. Min. Sci. 70, 343–352. https://doi.org/10.1016/j.ijrmms.2014.04.006.
Wen, T., Tang, H., Huang, L., Hamza, A., Wang, Y., 2020. An empirical relation for parameter mi in the Hoek–Brown criterion of anisotropic intact rocks with consideration of the minor principal stress and stress-to-weak-plane angle. Acta Geotech. https://doi.org/10.1007/s11440-020-01039-y.
Zhao, X.G., Cai, M., 2010. A mobilized dilation angle model for rocks. Int. J. Rock Mech. Min. Sci. 47, 368–384. https://doi.org/10.1016/j.ijrmms.2009.12.007.